AGU PUBLICATIONS

Geophysical Research Letters

RESEARCH LETTER
10.1002/2017GL076533

**Key Points:**
- A new inversion method for InSAR time series that considers all pixels simultaneously
- Incorporates a distance-dependent covariance between pixels to describe atmospheric noise
- Allows reconstruction of displacement rates from low-coherence data sets

**Supporting Information:**
- Supporting Information S1

**Correspondence to:**
R. Jolivet,
romain.jolivet@ens.fr

**Citation:**
Jolivet, R., & Simons, M. (2018). A multipixel time series analysis method accounting for ground motion, atmospheric noise, and orbital errors. *Geophysical Research Letters*, *45*, 1814–1824. https://doi.org/10.1002/2017GL076533

Received 24 NOV 2017
Accepted 5 FEB 2018
Accepted article online 9 FEB 2018
Published online 22 FEB 2018



# A Multipixel Time Series Analysis Method Accounting for Ground Motion, Atmospheric Noise, and Orbital Errors

**R. Jolivet**[1] **and M. Simons**[2]

[1]Laboratoire de Géologie, Département de Géosciences, École Normale Supérieure, CNRS UMR 8538, PSL Research University, Paris, France, [2]Seismological Laboratory, Departement of Geological and Planetary Sciences, California Institute of Technology, Pasadena, CA, USA

**Abstract** Interferometric synthetic aperture radar time series methods aim to reconstruct time-dependent ground displacements over large areas from sets of interferograms in order to detect transient, periodic, or small-amplitude deformation. Because of computational limitations, most existing methods consider each pixel independently, ignoring important spatial covariances between observations. We describe a framework to reconstruct time series of ground deformation while considering all pixels simultaneously, allowing us to account for spatial covariances, imprecise orbits, and residual atmospheric perturbations. We describe spatial covariances by an exponential decay function dependent of pixel-to-pixel distance. We approximate the impact of imprecise orbit information and residual long-wavelength atmosphere as a low-order polynomial function. Tests on synthetic data illustrate the importance of incorporating full covariances between pixels in order to avoid biased parameter reconstruction. An example of application to the northern Chilean subduction zone highlights the potential of this method.

## 1. Introduction

The development of time series analysis methods for interferometric synthetic aperture radar (InSAR) has led to significant advances in various fields of earth sciences. Large ground displacements are now routinely measured by combining single pairs of SAR images into interferograms, a measure of the spatial and temporal change of distance between the ground and an imaging satellite (e.g., Goldstein et al., 1993; Massonnet et al., 1993). For such measurements, the phase signature of the spatial and temporal variability in the refractivity gradients in the atmosphere often behaves as the dominant source of coherent noise (Doin et al., 2009; Hanssen, 2001; Hanssen et al., 1999). In addition, spatial and temporal decorrelation prevents the measure of a continuous displacement field over rough terrains, vegetated areas, or snow-covered regions, challenging attempts to measure ground displacements in many interferograms (Li & Goldstein, 1990; Zebker & Villasenor, 1992).

Time series analysis methods have been developed in order to reconstruct the spatial and temporal evolution of surface displacements from a stack of interferograms despite spatially and temporally variable interferometric phase coherence and to limit the impact of noise imposed by atmospheric delays (e.g., Agram et al., 2013; Berardino et al., 2002; Hetland et al., 2012; Usai, 2003). For instance, in the field of active tectonics, these methods allow detection of transient slip along active faults or to image slow, long-wavelength, strain rates due to interseismic loading across active faults (e.g., Bekaert et al., 2015; Daout et al., 2016; Elliott et al., 2008; Jolivet et al., 2012, 2013; Rousset et al., 2016).

Existing time series analysis methods can be classified into two groups: Persistent scatterer (PS) and temporally parameterized methods. PS techniques identify sets of pixels based on their scattering properties to improve the signal-to-noise ratio of interferograms and help phase unwrapping (e.g., Ferretti et al., 2001; Hooper et al., 2007, 2012). These methods are out of the scope of the present study as they work on a restricted set of pixels. In the following, we will only consider parameterized methods that include all unwrapped pixels of a set of interferograms to reconstruct the time-dependent interferometric phase. SBAS (Small Baseline Subset) methods concentrate on the evolution of the phase through time from a network of unwrapped interferograms, solving the set of linear equations relating the increments of phase with time to that of interferograms

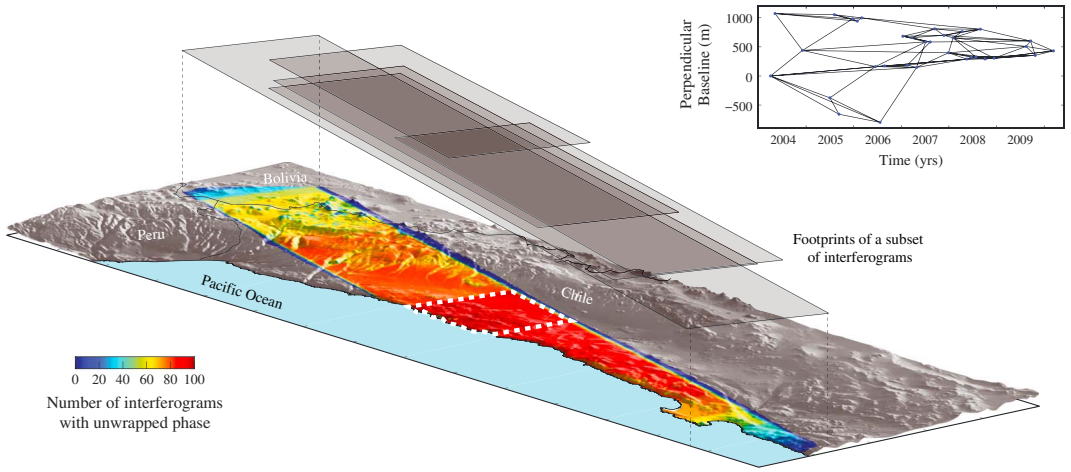


**Figure 1.** Illustration of the challenge of variable along-track coverage in synthetic aperture radar (SAR) interferometry. Color indicates the number of unwrapped pixels in the stack of interferograms computed from Envisat advanced SAR acquisitions along the northern Chilean coast on track 368. Gray rectangles indicate the along-track extent of five randomly selected interferograms out of the 96 total interferograms processed (see the baseline versus time plot on the upper-right for a description of the processed interferograms). Since the along-track extent of SAR acquisitions varies, so does the extent of the resulting interferograms, leaving a small area where all interferograms have been unwrapped (dashed white rectangle). Topography is from Shuttle Radar Topography Mission (Farr & Kobrick, 2000).

considering a constant velocity between acquisitions (Berardino et al., 2002). Multiple variants of SBAS have been proposed. Some concentrate on the actual phase values (Schmidt & Burgmann, 2003),while other methods focus on a geophysically motivated dictionary of time-dependent functions to describe the evolution of the phase (e.g., Agram et al., 2013, Hetland et al., 2012). The NSBAS (New Small Baseline Subset) approach combines both SBAS and a dictionary approach to overcome limitations posed by spatial and temporal decorrelation (López-Quiroz et al., 2009). All these methods require some level of a priori knowledge on the evolution of surface displacements in the case of disconnected subsets of interferometric pairs. In addition, all SBAS-based methods require careful prior removal of residual long-wavelength signals, including those due to orbital uncertainties or long-wavelength atmospheric perturbations (Doin et al., 2009).

While these methods provided the foundations for significant advances, several technical issues remain. SAR images in existing archives, such as those from the Envisat, ERS, or RadarSAT satellites, provide an invaluable data set to extend in the past 20 years current time series of deformation, especially when no ground-based geodetic data have been collected. However, images in these archives do not always cover the same area for technical reasons. For instance, in places like northern Chile, interferograms used as an input to any time series analysis method are built from acquisitions of variable along-azimuth coverage (Figure 1). In such case, a PS method cannot be systematically applied. Furthermore, if the extent of the area covered by all acquisitions is relatively small, it may be difficult to set differential interferograms in a common reference (i.e., a common set of pixels set to a common value) prior to an analysis with an SBAS-based time series method. In most methods, pixels are considered independent from each other despite known sources of correlated noise. For instance, the turbulent component of atmospheric delays can be statistically described by an empirical covariance function of the pixel-to-pixel distance (e.g., Chilès & Delfiner, 1999; Emardson et al., 2003; Jolivet et al., 2012; Lohman & Simons, 2005; Sudhaus & Jónsson, 2009). Ignoring this covariance will bias the inversion procedure. A potential solution is to perform the time series analysis in the wavelet domain in which wavelets are considered independent (Hetland et al., 2012; Shirzaei, 2013). However, this assumption still remains an approximation. In what follows, we describe a time series analysis method that allows one to consider all pixels simultaneously, reconstructing the temporal evolution of the interferometric phase in a common reference frame and accounting for spatial covariances in interferograms.

## 2. An Algorithm for Multipixel Time Series

### 2.1. Three Time Series Analysis Formulation

Reconstructing the evolution of the interferometric phase with time requires defining a common reference frame while estimating the evolution of the phase. The interferometric phase is the difference between phase

values at each acquisition. Due to its common appearance, many long-wavelength signals such as those from orbits, long-wavelength tropospheric perturbations, or oscillator drift (Fattahi & Amelung, 2014; Marinkovic & Larsen, 2013) have been commonly mistaken for orbital errors and are commonly empirically removed prior to time series analysis. Here, for simplicity, we describe this signal as a linear function of range and azimuth for each acquisition, hereafter referred to as the ramp. In addition to this ramp, we assume that interferograms are in a different reference frame that needs to be estimated in order to reconstruct continuous deformation fields. Therefore, for a pixel of coordinates $(x, y)$ in the range and azimuth reference frame, the interferometric phase $\Phi_{m,n}(x, y)$ combining two acquisitions at times $t_m$ and $t_n$ can be

$$\begin{aligned}\Phi_{m,n}(x,y) = \varphi_m(x,y) - \varphi_n(x,y) \\ + a_m x + b_m y - a_n x - b_n y + r_{m,n},\end{aligned} \tag{1}$$

where $\varphi_m(x, y)$ is the phase at a pixel $(x, y)$ and at an acquisition $m$ at a time $t_m$, and $a_m$ and $b_m$ are the parameters of the ramp at acquisition $m$ (and the equivalent for acquisition $n$). The last term, $r_{m,n}$, is the correction required to put each interferogram in a common reference frame. The difference between the three time series methods considered in the following lies in the formulation of the phase, $\varphi_m(x, y)$, as a function of time. We propose three approaches to solve this problem and reconstruct the evolution of deformation from a set of interferograms: a SBAS-based method, a dictionary-based method, and a NSBAS-based method.

Our implementation of the SBAS-based method solves for the phase values at each acquisition time with the formulation of Schmidt and Burgmann (2003). We solve equation (1) to recover the unknown parameters, including the 2-D fields $\varphi_m(x, y)$, the ramp parameters, $a_m$, $b_m$, and the referencing term $r_{m,n}$.

Our implementation of the dictionary method solves for the parameters of a time-dependent function, similarly to the approach proposed in the wavelet domain by Hetland et al. (2012) or in the space domain in the Generic Interferometric Toolbox (Agram et al., 2013). This approach is frequently used in the postprocessing of Global Navigation Satellite Systems time series. We write the phase at each acquisition, $\varphi_m(x, y)$, as the sum of a set of predefined functions. This set of functions may include a secular term (i.e., a linear function of time), periodic functions to account for seasonal or higher-order terms, spline functions to account for transient events, and Heaviside functions to model sudden ground motion like that due to earthquakes. The phase $\varphi_m(x, y)$ for a pixel of range and azimuth coordinates $(x, y)$ at time $t_m$ becomes

$$\begin{aligned}\varphi_m(x,y) = k(x,y) + v(x,y)t_m + \sum_{i=1}^{n_p}\left[c_i(x,y)\cos(2\pi\omega_i t_m) + s_i(x,y)\sin(2\pi\omega_i t_m)\right] \\ + \sum_{i=1}^{n_b} b_i(x,y)B_s(t_m - T_i) + \sum_{i=1}^{n_e} h_i(x,y)\mathcal{H}(t_m - T_i) + \ldots\end{aligned} \tag{2}$$

where $k(x, y)$ is a two-dimensional field of offsets, $v(x, y)$ is a field of phase velocity, $c_i(x, y)$ and $s_i(x, y)$ are the amplitudes of periodic oscillations, $b_i(x, y)$ are the amplitudes of spline, and $h_i(x, y)$ are the amplitudes of Heaviside functions. In this formulation, $n_p$, $n_b$, and $n_e$ are the number of periodic functions, of splines, and of Heaviside functions centered on time $T_i$, respectively. Here we solve equation (1), substituting the phase values $\varphi_m(x, y)$ by their formulation given in equation (2). Unknowns are the terms before each of the basis functions, the ramp parameters, and the referencing term. This method requires a geophysically motivated dictionary of functions to capture essential physical processes.

The NSBAS method aims at reconstructing the phase at each acquisition with the simultaneous estimation of a modeled phase history, combining both methods previously described (Daout et al., 2017; Doin et al., 2015; Jolivet et al., 2012; López-Quiroz et al., 2009). The addition of a set of function dictionary to adjust to the phase evolution allows to link temporally disconnected subsets in the case of low coherence. If for one pixel, subsets of the interferometric network are disconnected (i.e., no interferometric link constrains the phase evolution during that period) and there is no temporal overlap between the subnetworks, it is not possible to connect these phase histories with the SBAS approach. In this case, a function parameterized in time adjusted on the phase allows to connect the subsets (for some discussion on the subject, see Jolivet, 2011; López-Quiroz et al., 2009). Our implementation of the NSBAS-based method solves both equations (1) and (2) simultaneously. Unknowns are the phase fields, $\varphi_m(x, y)$, the ramp parameters, the referencing term, and the terms before the basis functions in equation (2). NSBAS has the advantage of providing a temporal evolution of the phase consistent with a parameterized model of surface displacements at once (i.e., we solve for the phase and fit it with some functions at once).

The three proposed methods are a variation of the same problem. If there are no disconnected subsets and all pixels concerned are unwrapped in each interferogram of the network, the SBAS-based and NSBAS-based approaches should yield identical phase fields and the dictionary and NSBAS-based approaches should result in identical fields of basis function terms. The choice of the method to employ will therefore depend on the configuration of the interferometric network and the specificities of the ground displacements and should be made on a case-by-case basis. Finally, we note that equation (1) is ill-posed. We therefore always solve the problem with respect to a reference in time (see supporting information S1).

### 2.2. Formulation of the Inverse Problem

Reconstructing the evolution of the phase through time consists of solving a linear inverse problem. We write

$$\mathbf{d} = \mathbf{G}\mathbf{m}, \tag{3}$$

where $\mathbf{d}$ is the data vector that contains the interferometric phase values for all the available pixels, $\mathbf{m}$ is the model vector of unknown parameters, and $\mathbf{G}$ is the matrix mapping the model space into the data space. The data vector has a size equal to the number of interferograms times the number of pixels. For instance, for a stack of 100 interferograms, with each containing about 1,000 pixels in range and in azimuth (i.e., roughly the size of an Envisat or ERS interferogram looked down 20 times in azimuth and 4 times in range), the data vector will contain 1E8 elements. For a similar sized problem, the number of unknowns depends on the method used but is on the order of 1E6 to 1E7 elements. The matrix $\mathbf{G}$ is large. However, it is also sparse and thus approachable with a distributed implementation.

We solve the inverse problem by finding model parameters $\mathbf{m}$ that minimize the generalized least square cost function $S$, defined as

$$2S(\mathbf{m}) = (\mathbf{G}\mathbf{m} - \mathbf{d})^T \mathbf{C}_\mathrm{d}^{-1} (\mathbf{G}\mathbf{m} - \mathbf{d}) + (\mathbf{m} - \mathbf{m}_\mathrm{prior})^T \mathbf{C}_\mathbf{m}^{-1} (\mathbf{m} - \mathbf{m}_\mathrm{prior}), \tag{4}$$

where $\mathbf{C}_\mathrm{d}$ and $\mathbf{C}_\mathrm{m}$ are the prior data and model covariance matrices and $\mathbf{m}_\mathrm{prior}$ the prior model (Tarantola, 2005). The prior data covariance matrix describes the uncertainties on the data, while the prior model covariance matrix describes our prior knowledge on the model parameters. This inverse problem has an analytical solution with the posterior model $\mathbf{m}_\mathrm{post}$ given by,

$$\mathbf{m}_\mathrm{post} = \mathbf{m}_\mathrm{prior} + \left(\mathbf{G}^t \mathbf{C}_\mathrm{d}^{-1} \mathbf{G} + \mathbf{C}_\mathrm{m}\right)^{-1} \mathbf{G}^t \mathbf{C}_\mathrm{d}^{-1} (\mathbf{d} - \mathbf{G}\mathbf{m}_\mathrm{prior}). \tag{5}$$

However, given the structure of the prior data and model covariance matrices described below, we cannot compute the second derivative of the cost function called Hessian, $\mathcal{H}$, that writes

$$\mathcal{H} = \mathbf{G}^T \mathbf{C}_\mathrm{d}^{-1} \mathbf{G} + \mathbf{C}_\mathrm{m}^{-1} \tag{6}$$

in the case of a linear problem; hence, we cannot compute $\mathbf{m}_\mathrm{post}$ directly (Tarantola, 2005). We solve this problem using a conjugate direction solver to iteratively approach $\mathbf{m}_\mathrm{post}$. Our fully parallel implementation uses the PETSc library and the mpi4py and petsc4py Python wrappers (Balay et al., 1997, 2016; Dalcin et al., 2011).

### 2.3. Choosing Covariances for Each Method

The choice of data and model covariances depends on the time series approach chosen. We provide general considerations based on our own experience and data sets and describe our implementation for the data and model covariances.

In both the SBAS and NSBAS approaches, we reconstruct the time evolution of the phase. In our approach, reconstructed phase still contains signals from all known and unknown sources of noise, such as phase noise or turbulent tropospheric perturbations. Therefore, as $\mathbf{C}_\mathrm{d}$ describes the uncertainty on the interferometric phase, it is necessary to build the data covariance matrix as a diagonal matrix with small values with respect to the expected precision of the reconstruction. In the dictionary approach and in the NSBAS approach, we interpret the evolution of the phase with a parameterized function of time. Therefore, the data covariance should reflect the influence of these various sources of noise.

For an interferogram, once the topography-correlated component of the atmospheric delay has been corrected for and assuming the remaining noise related to turbulent atmospheric delays is isotropic and spatially stationary, noise can be statistically described by a simple covariance function. This covariance function can be approximated by an exponential decay function of the distance between two pixels (Figure 2; Sudhaus & Jónsson, 2009; Jolivet et al., 2012). The covariance function, $C(x)$, can be written as

$$C(x) = \frac{1}{N(x)} \sum_{|i,j|_2 = x} |\Phi_i \Phi_j| \approx \sigma^2 e^{-x/\lambda}, \tag{7}$$

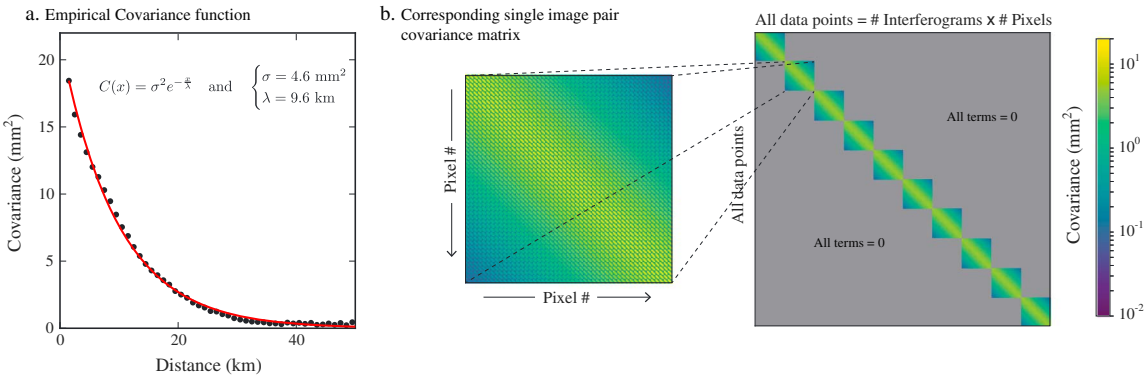


**Figure 2.** Prior data covariance. (a) Example of an empirical data covariance function determined on an interferogram (black dots) and the corresponding approximate exponential decay (red line). (b) This covariance function is used to build the covariance matrix of a single interferogram, which is then assembled with that from other interferograms to build the main covariance matrix of (c) the multipixel time series problem.

where $i$ and $j$ are two pixels of phase $\Phi_i$ and $\Phi_j$, $N(x)$ is the number of pixels separated by a distance $x$, and $\sigma$ and $\lambda$ are the amplitude and the characteristic length scale of the approximate covariance function. We compute the empirical covariance function of each interferogram and approximate these covariances by a best fit exponential decay (equation (7)). We use these functions to build the data covariance matrix. In the NSBAS approach, the basis function terms are adjusted to the phase at each acquisition date. We therefore reconstruct the amplitude and characteristic length scales of the noise covariance function for each acquisition through time series analysis.

Although model covariance primarily aims at managing the ill-posedness of the problem through damping or smoothing, building the prior model covariance matrix $\mathbf{C}_\mathrm{m}$ requires a decision motivated by the physics of the surface processes measured. We assume that ramp and reference parameters are independent from all other parameters, hence a diagonal covariance matrix. The value of the diagonal term depends on the set of interferograms, but should be large with respect to what is to be expected. Then, one of the goals of this multipixel time series analysis method is to derive spatially continuous phase and function parameter fields in regions where coherence is not particularly optimal. Therefore, it is necessary to include some prior correlation, or smoothing, between pixels in our prior model covariance matrix. In other words, using a diagonal prior model covariance matrix would be similar to a pixel-by-pixel approach. We build the model covariance matrix using the covariance function of equation (7) to impose a prior correlation between the model parameters. In any case, the amplitude of the model covariance should be large compared to the expected values. We note that in the case of interferograms with full spatial coverage and no missing pixels, one should consider a model covariance as uninformative as possible, hence no off-diagonal terms.

### 2.4. Prior Model and Data Covariances

In both the dictionary and NSBAS approaches, a part of the data covariance matrix is formed as a block diagonal matrix, with each block corresponding to a single image pair (dictionary approach) or to an acquisition (NSBAS approach) (Figure 2). Unfortunately, each block has dimensions equal to the square of the number of pixels. Furthermore, each block is not sparse, making the explicit formulation of these matrices and computing their inverse impractical. A part of the model covariance matrix is also block diagonal with each block of dimension equal to the square of the number of pixels, making once again the handling of such matrix impractical.

Matrix-vector multiplication and matrix inversion are straightforward in the case of diagonal matrices, but challenging for large, nonsparse covariance matrices. For these reasons, we cannot compute directly the aforementioned Hessian term of the generalized solution to the least squares problem (equation (5)). However, the multiplication of a 2-D field by a covariance matrix is equivalent to a convolution in the space domain, thus a multiplication in the Fourier domain (Oliver, 1998). For a large, nonsparse covariance matrix $\mathbf{C}$ built from a function $K(x, y)$, and given a 2-D field $\Phi$ rearranged in a vector $\mathbf{v}$, we write

$$\mathbf{Cv} = K * \Phi = \int_{-\infty}^{\infty}\int_{-\infty}^{\infty} K(\mathbf{x}-x', \mathbf{y}-y')\Phi(\mathbf{x},\mathbf{y})\mathrm{d}x'\mathrm{d}y' \tag{8}$$

where **x** and **y** are the coordinates of the field and $x'$ and $y'$ are integration variables. The multiplication by the inverse of a covariance matrix is equivalent to the convolution by a function $G$ so that, in the Fourier domain, $\hat{K}\hat{G} = 1$ where $\hat{G}$ denotes the Fourier transform of $G$ (Oliver, 1998). If we consider a 2-D covariance kernel, $K$, depending on two positive real numbers $\sigma$ and $\lambda$, so that

$$\forall (x, y) \in \mathbb{R}^2, \quad K(x, y) = \sigma^2 e^{-\frac{\sqrt{x^2 - y^2}}{\lambda}} \tag{9}$$

then its Fourier transform is given by

$$\forall (u, v) \in \mathbb{R}^2, \quad \hat{K}(u, v) = \frac{2\pi\lambda^2\sigma^2}{(1 + \lambda^2 u^2 + \lambda^2 v^2)^{3/2}} \quad \text{and} \quad \hat{G} = \frac{1}{\hat{K}} \tag{10}$$

as shown by Oliver (1998). This convolution with $K$ given in equation (9) amounts to a smoothing operation (i.e., damping high frequencies) while the convolution with $G$ is a roughening operation. Interferograms can be considered independently from each others as temporal covariance are negligible given the repeat time of acquisitions (Emardson et al., 2003). Therefore, we replace all matrix vector products involving such covariance in our conjugate direction solver by a convolution of the two-dimensional phase or model fields with the exponential function given in equation (7). Details on the conjugate gradient method and performance of the covariance matrix convolution are described in the supporting information.

## 3. Solving Strategies, Synthetic Tests, and Real Data

### 3.1. Tests on a Synthetic Data Set

To validate our approach, we construct a synthetic set of interferograms based on the interferometric network of the set of Envisat interferograms available for track 368 in northern Chile (Figure 1). The synthetic time series of displacement is 6 years long with 33 acquisitions. We construct a total of 96 interferograms. The resulting size of each interferogram is 177 pixels wide for 1,264 pixels long (i.e., corresponding to the range and azimuth length in pixels of an Envisat interferogram with 80 looks in azimuth and 16 looks in range). In order to construct the phase evolution with time of a pixel of range and azimuth coordinates $x$ and $y$, we use the time-dependent function, $f(x, y, t)$, combining a linear term, a step in time, and a logarithmic decay with time:

$$f(x, y, t) = v(x, y)t + h(x, y)\mathcal{H}(t, T_e) + l(x, y)\mathcal{H}(t, T_e)\log\left(1.0 + \frac{t - T_e}{\tau}\right) \tag{11}$$

$$\text{with} \quad \begin{cases} \mathcal{H}(t, T_e) = 0 & \text{if} \quad t < T_e \\ \mathcal{H}(t, T_e) = 1 & \text{if} \quad t > T_e \end{cases} \tag{12}$$

where $v(x, y)$ is the amplitude of the 2-D velocity field, $h(x, y)$ is the amplitude of the imposed step function, and $l(x, y)$ is the amplitude of the logarithmic decay with time (Figure 3).

In order to simulate realistic phase values, we add noise to each of the images of the time series. For each acquisition, we build a random realization that follows an exponentially decaying covariance function (equation (9) with $\sigma = 0.3$ and $\lambda = 10$ pixels) by the convolution of a white noise and this exponential decay in 2-D. For each acquisition, we build a random linear function of range and azimuth from a uniform distribution to simulate the effect of random long-wavelength perturbations such as orbital uncertainties. Finally, in order to simulate the effect of variable spatial coverage of interferograms, we include a variable decoherence pattern for each acquisition. We build this random pattern for each interferogram by masking out pixels for which a random realization of correlated noise exceeds a specific value (for an example of synthetic interferogram, see supporting information S1). Final spatial coverage for each interferogram ranges between 50 and 90% of the total number of pixels.

The goal is to verify that we can reconstruct both phase evolution and parameters of the dictionary of functions. As the conjugate gradient solver may converge very slowly, we proceed in several steps to accelerate the convergence. We first run the dictionary approach with a function combining a secular rate, a step, and a logarithmic function starting from a prior model in which all terms are equal to zero. We use a data covariance based on an exponential function equal to that of the synthetic noise we have introduced. The prior model covariances for all the parameters are also exponential functions with a large variance. Model priors for the ramp and reference parameters are uncorrelated. Using the obtained model parameters, we compute the temporal evolution of the phase and use these both as initial values and as prior model for the conjugate gradient solver in the NSBAS method. Model covariance is a diagonal matrix for the phase part of the model

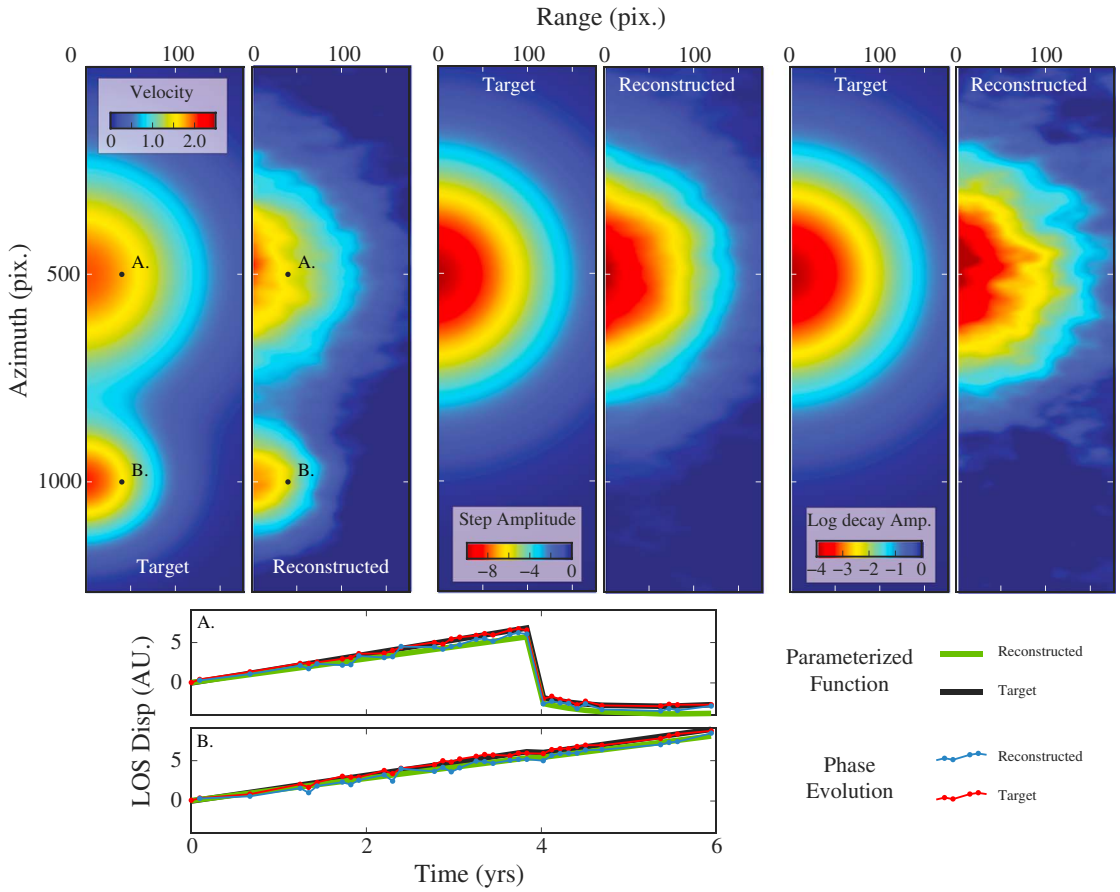


**Figure 3.** Performance on a synthetic data set. Target and reconstructed function parameter and phase fields for the case of a synthetic data set using the NSBAS approach. The synthetic data set includes a constant velocity term (left), a step function (middle), and a logarithmic decay (right). Bottom plots show the temporal evolution of the phase of two pixels A and B identified on the velocity field. The shape of each of these fields is based on a 2-D Gaussian function. LOS = line of sight.

space and an exponential covariance for the functional part. Covariance for the orbital terms is unchanged. Covariances are summarized in the supporting information.

The final results for the NSBAS method compare relatively well with the target model, although we point out some differences (Figure 3). The reconstructed model fields are slightly different as they are more rough than the target model. Furthermore, the amplitude of the velocity field is slightly smaller, leading to greater inconsistencies between model and target at the end of the time series. These differences are mainly due to the ill-posedness of the problem caused by variable spatial phase coherence and the correlation between ramp terms and model fields. When solving for a synthetic case where we include no variable spatial coherence (i.e., all pixels are unwrapped) and no ramp terms, the model is almost perfectly recovered. Similarly, when no correlated noise is added, the inversion recovers the target exactly. Further exploration of the influence of the amplitude of tropospheric noise and its potential variability in time should now be considered.

### 3.2. Application to Northern Chile

We illustrate our method by reconstructing the evolution of surface displacements in northern Chile along track 368 of the Envisat satellite between 2003 and 2010. We compute 96 interferograms with a final pixel size of 650 m (16 looks in range and 80 looks in azimuth) from 33 acquisitions using the NSBAS processing chain, based on the ROI_PAC software (Doin et al., 2011; Rosen et al., 2004). Processing is detailed in Doin et al. (2011) and in Jolivet et al. (2012). We use the GIAnT and PyAPS softwares to correct interferograms from the stratified component of atmospheric perturbations using the predictions from the ERA-Interim reanalysis (Agram et al., 2013; Dee et al., 2011; Jolivet et al., 2011). ERA-Interim allows to correct for long-wavelength, topography-correlated atmospheric delays. Shorter wavelength, turbulent components of the atmospheric delay are hence not well corrected for and can be considered stochastically in the inversion. Our goal is to

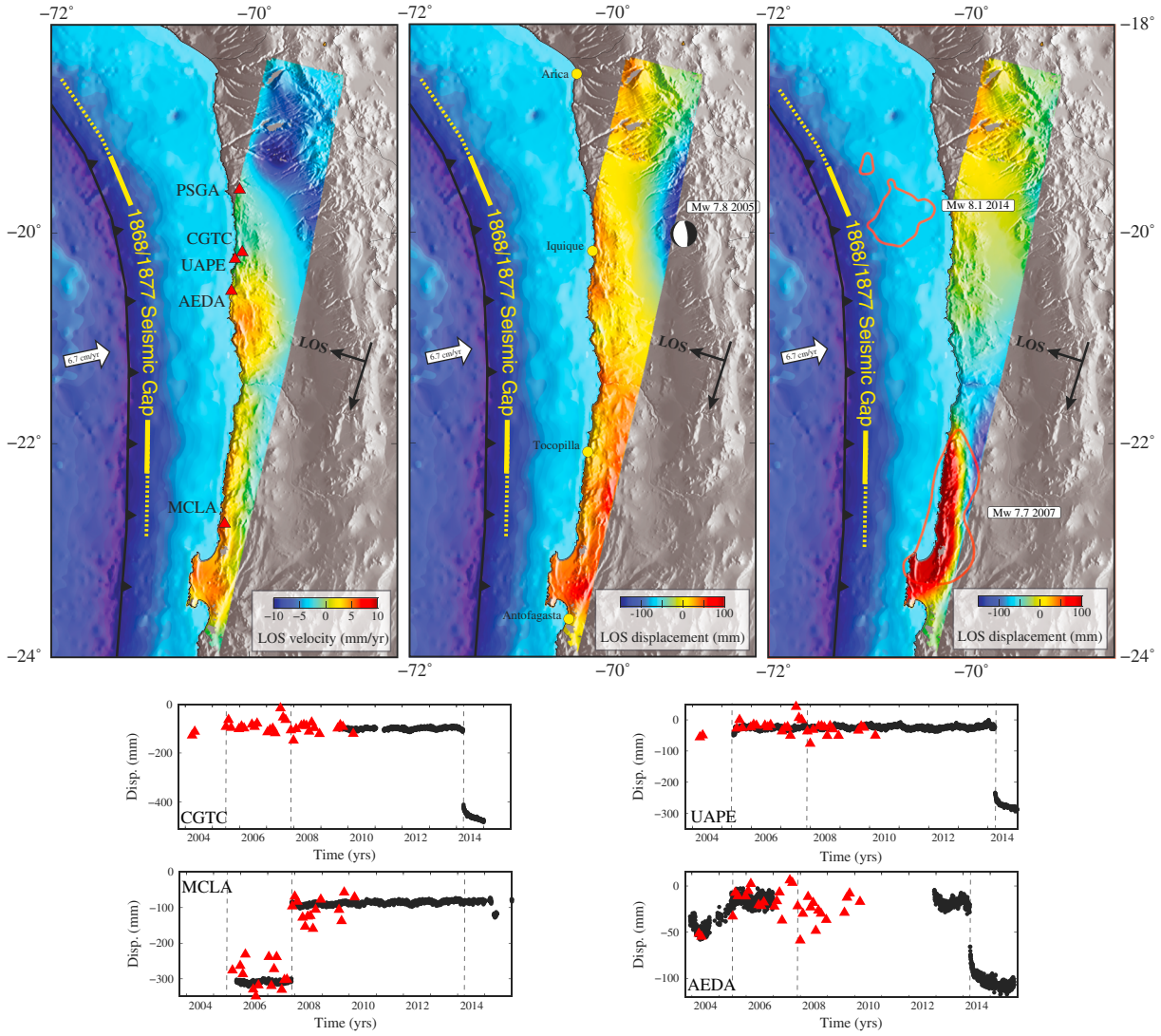


**Figure 4.** Inversion results for the NSBAS method in northern Chile. (top left) The reconstructed field of interseismic displacement rate assumed constant for the period of observation. (top middle) The reconstructed coseismic displacement field for the 2005 $M_w$ 7.8 Tarapaca deep-focal earthquake. (top right) The reconstructed coseismic displacement field for the 2007 $M_w$ 7.7 Tocopilla earthquake. Red lines indicate the 3 m and 50 cm contour for the 2007 $M_w$ 7.7 Tocopilla and 2014 $M_w$ 8.1 Pisagua earthquakes, respectively. Time series plots show the comparison between GPS time series (black dots) and our reconstructed interferometric synthetic aperture radar time series (red triangles) for four sites shown as red triangles on the velocity map. All GPS displacements are referenced to those of site PSGA. Dashed lines indicate the 2005, 2007, and 2014 earthquakes. LOS = line of sight.

solve the NSBAS problem using an approach similar to the synthetic test shown in the previous section. In order to facilitate the convergence of the solver, we first run the dictionary approach, then the SBAS problem using the predicted phase values as a starting point and prior model and finally the NSBAS problem with the inferred parameters as a starting point and prior model. Our parameterized function is the sum of a linear trend, two Heaviside functions for the 2005 $M_w$ 7.8 Tarapaca and 2007 $M_w$ 7.7 Tocopilla earthquakes and a periodic oscillation of 1 year period. Data covariances are estimated directly on the input interferograms. Model covariances are set to exponential functions. Covariance structures and run performances are summarized in the supporting information.

We reconstruct the coseismic displacement fields for both $M_w$ 7+ earthquakes in the area and extract a continuous velocity field over a large area, despite the relatively poor overlap between all the interferograms. We reconstruct about 10 cm of surface subsidence during the Tarapaca earthquake consistent with published models for this earthquake for the spatial coverage allowed by track 368 (Peyrat et al., 2006). Surface displacements range from −15 cm to more than 20 cm toward the satellite along the line of sight for the Tocopilla

earthquake (Bejar-Pizarro et al., 2010). The velocity field is comparable to those measured and predicted by Béjar-Pizarro et al. (2013) although with slight lateral differences. We validate our reconstructed displacement time series by projecting the displacements measured at cGPS sites in the line of sight of the satellite and comparing with the displacements averaged over a 4 km radius surrounding the stations (Figure 4). Our time series, although noisier, agree well with the projected time series of displacement measured by GPS. In particular, we note that time series at CGTC, a site almost collocated with UAPE, illustrate the potential of InSAR archive to extend in the past records from recently installed cGPS stations.

## 4. Discussion

It is worth considering different cases in which each of the approaches proposed in this paper are appropriate. SBAS aims at reconstructing the phase with great accuracy, including the effect of propagation delays. The dictionary approach aims at directly providing a geophysical interpretation of the interferometric phase in space and time. In a case where all pixels are unwrapped with no disconnected subsets, reconstructing the phase using the SBAS approach and then fitting it with a parameterized function of time is equivalent to solving the dictionary approach. In such case, the NSBAS approach would not provide any advantage. In the same case, imposing an exponential form as a prior model covariance only restricts the range of possible phase reconstructions via SBAS and pixels should then be considered independently. However, issues arise when fractions of interferograms are not unwrapped, leaving holes both in space and time in our observation of ground displacements. In this common case, we should use the covariance between pixels to propagate information in space and NSBAS can be an effective solution to bridge gaps in time if we want to reconstruct the phase history. The method proposed is therefore most appropriate for the exploitation of archive data from past constellations of satellite and from recent constellations over areas of low coherence or with variable coherence such as due to seasonal snow cover.

The main limitation of our approach lies in the choice of $\mathbf{C}_m$. Choosing large variances suggests that the prior model is not to be trusted and allows the conjugate gradient solver the freedom to converge toward the best possible model. Including exponential covariances restricts the choice of possible models to spatially smooth deformation fields hence provides necessary constraints for the ramp parameters. All these choices can be physically justified, but many combinations should be tested, as the results may depend on these choices. In particular, we have only presented the case of exponential covariances but any function with an analytical formulation in the Fourier domain can be used. Some exceptions remain since, for instance, in the case of a Gaussian covariance kernel, the inverse convolution leads to an exponential increase of high frequencies, hence the need for an adequate damping of high frequencies prior to the convolution.

The algorithm presented here is also limited by the efficiency of the conjugate direction solver. The number of iterations to run before the cost function, $S(\mathbf{m})$, reaches a minimum can be prohibitive in some cases. In addition, given the accuracy we aim for at the reconstruction of the phase values in the NSBAS hybrid method, there is a significant imbalance in the amplitude of the phase terms versus the model terms in the steepest descent vector at each iteration. Therefore, at each step the solver moves very slowly along the dimensions of the model space corresponding to the parameters of the dictionary functions, while convergence is quite fast toward a reasonable phase evolution. This issue can be avoided by proceeding in steps such as first solving the dictionary approach and then solving for the NSBAS hybrid problem, as we proposed in our validation section.

An improved approach would use a Newton algorithm. Instead of using the local gradient to determine the direction at each iteration, Newton algorithms approximate a local parabola tangential to the cost function. In the case of a linear problem, the cost function is parabolic and the Newton algorithm converges in a single iteration. Newton methods require computation of the Hessian, $\mathcal{H}$ and its inverse and, given the formulation of our covariance matrices, we cannot do so. One solution would be to explore the potential of hierarchical matrix methods to compute the Hessian and, in a more general sense, to speed up the steepest ascent vector computation (e.g., Desiderio, 2017).

## 5. Conclusion

We have presented an implementation of existing time series analysis methods augmented to handle full images at once rather than on a pixel-by-pixel basis. This improvement allows us to reconstruct surface

displacements from a set of interferograms with an automatic coreferencing of the data. We have developed an efficient way of accounting for atmospheric noise in the reconstruction of surface displacements via a Fourier domain covariance convolution substituted to the classic matrix vector products. This method allows us to handle very large problems and eventually derive time series from complex data sets where coherence varies significantly, challenging attempts to reference interferograms to a common reference frame, and provide estimates of velocities or any displacement field accounting for tropospheric noise. We show that in time series analysis, interferograms can be dealt with as full images with the appropriate statistical noise description.

**Acknowledgments**
We thank Angelyn Moore and Susan Owen for making the GPS time series available through the Aria project. We would like to thank N. Brantut for the fruitful discussions about inverse problems in general. M. S. was partially supported by NASA grant NNX16AK58G. This project has received funding from the European Research Council (ERC) under the European Union's Horizon 2020 research and innovation program (grant agreement 758210). This work was granted access to the HPC resources of MesoPSL financed by the Region Ile de France and the project Equip@Meso (reference ANR-10-EQPX-29-01) of the program Investissements d'Avenir supervised by the Agence Nationale pour la Recherche. Codes are available on our website with instructions for installation (https://www.geologie.ens.fr/~jolivet) along with examples. Envisat raw data have been obtained upon request via the EOLISA tool. We thank the European Space Agency for the acquisition and the distribution of these data. ERA-Interim products are directly available for download at ECMWF (https://www.ecmwf.int/).

## References

Agram, P. S., Jolivet, R., Riel, B., Lin, Y. N., Simons, M., Hetland, E., et al. (2013). New radar interferometric time series analysis toolbox released. *Eos*, *94*(7), 69–76. https://doi.org/10.1029/2011JB008731

Balay, S., Abhyankar, S., Adams, M. F., Brown, J., Brune, P., Buschelman, K., et al. (2016). PETSc users manual (Tech. Rep. ANL-95/11 - Revision 3.7). Argonne National Laboratory.

Balay, S., Gropp, W. D., McInnes, L. C., & Smith, B. F. (1997). Efficient management of parallelism in object oriented numerical software libraries. In S. Balay, W. D. Gropp, L. C. McInnes, & B. F. Smith (Eds.), *Modern Software Tools in Scientific Computing* (pp. 163–202). Birkhäuser Press.

Bejar-Pizarro, M., Carrizo, D., Socquet, A., Armijo, R., Barrientos, S., Bondoux, F., et al. (2010). Asperities and barriers on the seismogenic zone in North Chile: State-of-the-art after the 2007 $M_w$ 7.7 Tocopilla earthquake inferred by GPS and InSAR data. *Geophysical Journal International*, *183*(1), 390–406. https://doi.org/10.1111/j.1365-246X.2010.04748.x

Béjar-Pizarro, M., Socquet, A., Armijo, R., Carrizo, D., Genrich, J., & Simons, M. (2013). Andean structural control on interseismic coupling in the North Chile subduction zone. *Nature Geoscience*, *6*(5), 462–467. https://doi.org/10.1038/ngeo1802

Bekaert, D. P. S., Hooper, A., & Wright, T. J. (2015). Reassessing the 2006 Guerrero slow-slip event, Mexico: Implications for large earthquakes in the Guerrero Gap. *Journal of Geophysical Research: Solid Earth*, *120*, 1357–1375. https://doi.org/10.1002/2014JB011557

Berardino, P., Fornaro, G., Lanari, R., & Sansosti, E. (2002). A new algorithm for surface deformation monitoring based on small baseline differential SAR interferograms. *IEEE Transactions on Geoscience and Remote Sensing*, *40*(11), 2375–2383.

Chilès, J. P., & Delfiner, P. (1999). *Geostatistics—Modeling spatial uncertainty*, *Wiley Series in Probability and Statistics. Applied Probability and Statistics Section*. John Wiley.

Dalcin, L. D., Paz, R. R., Kler, P. A., & Cosimo, A. (2011). Parallel distributed computing using Python. *Advances in Water Resources*, *34*(9), 1124–1139. https://doi.org/10.1016/j.advwatres.2011.04.013, new Computational Methods and Software Tools.

Daout, S., Jolivet, R., Lasserre, C., Doin, M. P., Barbot, S., Tapponnier, P., et al. (2016). Along-strike variations of the partitioning of convergence across the Haiyuan fault system detected by InSAR. *Geophysical Journal International*, *205*, 536–547. https://doi.org/10.1093/gji/ggw028

Daout, S., Doin, M.-P., Peltzer, G., Socquet, A., & Lasserre, C. (2017). Large-scale InSAR monitoring of permafrost freeze-thaw cycles on the Tibetan Plateau. *Geophysical Research Letters*, *44*, 901–909. https://doi.org/10.1002/2016GL070781

Dee, D. P., Uppala, S. M., Simmons, A. J., Berrisford, P., Poli, P., Kobayashi, S., et al. (2011). The ERA-Interim reanalysis: Configuration and performance of the data assimilation system. *Quarterly Journal of the Royal Meteorological Society*, *137*(656), 553–597.

Desiderio, L. (2017). *H-matrix based solvers for 3D elastodynamic boundary integral equations*, (PhD thesis). Université Paris Saclay.

Doin, M. P., Lasserre, C., Peltzer, G., Cavalié, O., & Doubre, C. (2009). Corrections of stratified tropospheric delays in SAR interferometry: Validation with global atmospheric models. *Journal of Applied Geophysics*, *69*(1), 35–50. https://doi.org/10.1016/j.jappgeo.2009.03.010

Doin, M. P., Lodge, F., Guillaso, S., Jolivet, R., Lasserre, C., Ducret, G., et al. (2011). Presentation of the small baseline NSBAS processing chain on a case example: The Etna deformation monitoring from 2003 to 2010 using Envisat data. In *Proceedings of the Fringe symposium* (pp. 1–7). Frascati, Italy.

Doin, M.-P., Twardzik, C., Ducret, G., Lasserre, C., Guillaso, S., & Jianbao, S. (2015). InSAR measurement of the deformation around Siling Co Lake: Inferences on the lower crust viscosity in central Tibet. *Journal of Geophysical Research: Solid Earth*, *120*, 5290–5310. https://doi.org/10.1002/2014JB011768

Elliott, J. R., Biggs, J., Parsons, B., & Wright, T. J. (2008). InSAR slip rate determination on the Altyn Tagh Fault, northern Tibet, in the presence of topographically correlated atmospheric delays. *Geophysical Research Letters*, *35*, L12309. https://doi.org/10.1029/2008GL033659

Emardson, T. R., Simons, M., & Webb, F. H. (2003). Neutral atmospheric delay in interferometric synthetic aperture radar applications: Statistical description and mitigation. *Journal of Geophysical Research*, *108*(B5), 2231. https://doi.org/10.1029/2002JB001781

Farr, T. G., & Kobrick, M. (2000). Shuttle radar topography mission produces a wealth of data. *Eos, Transactions American Geophysical Union*, *81*(48), 583–585.

Fattahi, H., & Amelung, F. (2014). InSAR uncertainty due to orbital errors. *Geophysical Journal International*, *199*(1), 549–560. https://doi.org/10.1093/gji/ggu276

Ferretti, A., Prati, C., & Rocca, F. (2001). Permanent scatterers in SAR interferometry. *IEEE Transactions on Geoscience and Remote Sensing*, *39*(1), 8–20. https://doi.org/10.1109/36.898661

Goldstein, R. M., Engelhardt, H., Kamb, B., & Frolich, R. M. (1993). Satellite radar interferometry for monitoring ice sheet motion: Application to an Antarctic ice stream. *Science*, *262*(5139), 1525–1530.

Hanssen, R. F. (2001). *Radar interferometry, data interpretation and error analysis*, *Remote sensing and digital image processing*. Dortrecht, Netherlands: Kulwer Academic Publishers.

Hanssen, R. F., Weckwerth, T. M., Zebker, H. A., & Klees, R. (1999). High-resolution water vapor mapping from interferometric radar measurements. *Science*, *283*(5406), 1297–1299. https://doi.org/10.1126/science.283.5406.1297

Hetland, E. A., Musé, P., Simons, M., Lin, Y. N., Agram, P. S., & DiCaprio, C. J. (2012). Multiscale InSAR Time Series (MInTS) analysis of surface deformation. *Journal of Geophysical Research*, *117*, B02404. https://doi.org/10.1029/2011JB008731

Hooper, A., Bekaert, D., Spaans, K., & Arikan, M. (2012). *Recent advances in SAR interferometry time series analysis for measuring crustal deformation* (Vol. 514–517, pp. 1–13). https://doi.org/10.1016/j.tecto.2011.10.013

Hooper, A., Segall, P., & Zebker, H. (2007). Persistent scatterer interferometric synthetic aperture radar for crustal deformation analysis, with application to Volcán Alcedo, Galápagos. *Journal of Geophysical Research*, *112*, B07407. https://doi.org/10.1029/2006JB004763

Jolivet, R. (2011). *Déformation intersismique le long de la faille de Haiyuan, Chine: Variations spatio-temporelles contraintes pas interférométrie radar*, (PhD thesis). Université de Grenoble, France.

Jolivet, R., Grandin, R., Lasserre, C., Doin, M. P., & Peltzer, G. (2011). Systematic InSAR tropospheric phase delay corrections from global meteorological reanalysis data. *Geophys Research Letters*, *38*, L17311. https://doi.org/10.1029/2011GL048757

Jolivet, R., Lasserre, C., Doin, M. P., Guillaso, S., Peltzer, G., Dailu, R., et al. (2012). Shallow creep on the Haiyuan Fault (Gansu, China) revealed by SAR interferometry. *Journal of Geophysical Research*, *117*, B06401. https://doi.org/10.1029/2011JB008732

Jolivet, R., Lasserre, C., Doin, M. P., Peltzer, G., Avouac, J. P., Sun, J., & Dailu, R. (2013). Spatio-temporal evolution of aseismic slip along the Haiyuan fault, China: Implications for fault frictional properties, Earth Planet. *Science Letters*, *377–378*, 23–33. https://doi.org/10.1016/j.epsl.2013.07.020

Li, F. K., & Goldstein, R. M. (1990). Studies of multibaseline spaceborne interferometric synthetic aperture radars. *IEEE Transactions on Geoscience and Remote Sensing*, *28*(1), 88–97. https://doi.org/10.1109/36.45749

Lohman, R. B., & Simons, M. (2005). Some thoughts on the use of InSAR data to constrain models of surface deformation: Noise structure and data downsampling. *Geochemistry, Geophysics, Geosystems*, *6*, Q01007. https://doi.org/10.1029/2004GC000841

López-Quiroz, P., Doin, M.-P., Tupin, F., Briole, P., & Nicolas, J.-M. (2009). Time series analysis of Mexico City subsidence constrained by radar interferometry. *Journal of Applied Geophysics*, *69*, 1–15. https://doi.org/10.1016/j.jappgeo.2009.02.006

Marinkovic, P., & Larsen, Y. (2013). Consequences of long-term ASAR local oscillator frequency decay—An empirical study of 10 years of data. In *Living Planet Symposium*. Edinburgh, UK.

Massonnet, D., Rossi, M., Carmona, C., Adragna, F., Peltzer, G., Feigl, K., & Rabaute, T. (1993). The displacement field of the Landers earthquake mapped by Radar interferometry. *Nature*, *364*, 138–142.

Oliver, D. S. (1998). Calculation of the inverse of the covariance. *Mathematical Geology*, *30*(7), 1–23.

Peyrat, S., Campos, J., de Chabalier, J. B., Perez, A., Bonvalot, S., Bouin, M. P., et al. (2006). Tarapacá intermediate-depth earthquake ($M_W$ 7.7, 2005, northern Chile): A slab-pull event with horizontal fault plane constrained from seismologic and geodetic observations. *Geophysical Research Letters*, *33*, L22308. https://doi.org/10.1029/2006GL027710

Rosen, P. A., Hensley, S., Peltzer, G., & Simons, M. (2004). Updated repeat orbit interferometry PACkage released. *Eos, Transactions American Geophysical Union*, *85*(5), 47–47.

Rousset, B., Jolivet, R., Simons, M., Lasserre, C., Riel, B., Milillo, P., et al. (2016). An aseismic slip transient on the North Anatolian Fault. *Geophysical Research Letters*, *43*, 3254–3262. https://doi.org/10.1002/2016GL068250

Schmidt, D. A., & Burgmann, R. (2003). Time-dependent land uplift and subsidence in the Santa Clara valley, California, from a large interferometric synthetic aperture radar data set. *Journal of Geophysical Research*, *108*(B9), 2416. https://doi.org/10.1029/2002JB002267

Shirzaei, M. (2013). A wavelet-based multitemporal DInSAR algorithm for monitoring ground surface motion. *IEEE Geoscience and Remote Sensing Letters*, *10*(3), 456–460. https://doi.org/10.1109/LGRS.2012.2208935

Sudhaus, H., & Jónsson, S. (2009). Improved source modelling through combined use of InSAR and GPS under consideration of correlated data errors: Application to the June 2000 Kleifarvatn earthquake, Iceland. *Geophysical Journal International*, *176*(2), 389–404. https://doi.org/10.1111/j.1365-246X.2008.03989.x

Tarantola, A. (2005). *Inverse problem theory and methods for model parameter estimation*. Philadelphia, USA: SIAM.

Usai, S. (2003). A least squares database approach for SAR interferometric data. *IEEE Transactions on Geoscience and Remote Sensing*, *41*(4), 753–760.

Zebker, H. A., & Villasenor, J. (1992). Decorrelation in interferometric radar echoes. *IEEE Transactions on Geoscience and Remote Sensing*, *30*(5), 950–959.